Available online at www.sciencedirect.com
ScienceDirect
Journal of Molecular Catalysis A: Chemical 267 (2007) 57–64
JOURNAL OF MOLECULAR CATALYSIS A: CHEMICAL
www.elsevier.com/locate/molcata

Investigations on gold nanoparticles supported on rare earth oxide catalytic materials

Suresh K. Bhargava [a], Deepak B. Akolekar [a,*], Garry Foran [b]

[a] *Catalysis and Advanced Materials Research Group, Department of Applied Chemistry, RMIT University, City Campus, Melbourne, Victoria 3001, Australia*
[b] *Australian Synchrotron Research Program, c/o ANSTO, PMB 1, Menai, NSW 2234, Australia*

Received 15 September 2006; received in revised form 5 November 2006; accepted 6 November 2006
Available online 17 November 2006

Abstract

Supported gold nanoparticles rare earth (europium, dysprosium, samarium oxide, neodymium, gadolinium oxide and lanthanum oxide) materials were prepared using precipitation–deposition/co-precipitation methods. The techniques employed for the characterization of these materials were ICP-MS, TEM, XRD, BET, and XAS. Au L_3-edge X-ray absorption spectroscopic measurements were carried out over a series of rare earth materials containing gold nanoparticles. The size of gold nanoparticles varied in the range of ~2 to 6 nm in the Eu/Dy/Sm/Nd/Gd/La materials. These materials possess surface areas ranging from 29 to 41 m^2/g with the high phase purity and crystallinity of the support (Eu/Dy/Sm/Nd/Gd/La) materials. An X-ray absorption fine structure (XANES, EXAFS) technique was used in obtaining critical information about the atomic distances, bonding and neighbouring environment for gold atoms in the rare earth Eu/Dy/Sm/Nd/Gd/La oxide materials for understanding the typical characteristics and structure of gold nanoparticles in these materials.

Keywords: Gold nanoparticles; Rare earths; Eu; Sm; La; Nd; Gd; Dy; EXAFS; XANES; Surface properties

1. Introduction

In recent years research on a number of important catalytic materials have increased tremendously. Apart from transition metals support materials, rare earth elements have an important role in catalyst support development and they have their importance for their luminescent, photoconductive, photorefractive, superconducting, laser action and magnetic properties. Nano-structured materials with different support characteristics are of great interest in catalytic applications in the low-temperature catalytic combustion, partial oxidation of hydrocarbons, hydrogenation of carbon oxides and unsaturated hydrocarbons reduction of NO, etc. For nanoparticles, support materials play important role by providing high reactive surface area, thermal stability, higher dispersion of nano-metallic particles, longer catalyst life, and a structure sensitive base, etc. For development of good nanocatalytic materials, the structures and environment of nanoparticles are very critical and also, it is very important that the nanoparticles are properly stabilised in the support matrix [1–3].

Various literatures [4–7] have reported that gold particles active in a particular form/environment/size and distribution are responsible for certain types of oxidation/hydrogenation/hydrochlorination reactions and most reactions are noticeably structure sensitive over supported gold catalysts. Supported nano-gold catalysts are typically used in the low-temperature, catalytic combustion and partial oxidation of hydrocarbons, carbon monoxide, hydrogenation of carbon oxides and unsaturated hydrocarbons reduction of nitric oxide, etc. [4–7] and nano-gold catalysts provide fast reaction rate, high selectivity, and low reaction temperature [8].

The main aim of the research project was to investigate the structural properties of gold nanoparticles supported on different rare earth oxide (europium. dysprosium, samarium oxide, neodymium, gadolinium oxide, lanthanum) materials. High purity europium, dysprosium, samarium oxide, neodymium, gadolinium oxide and lanthanum oxide materials containing various loading of gold nanoparticles were prepared by different methods. X-ray absorption fine structure

* Corresponding author. Tel.: +61 3 99252121; fax: +61 3 96391321.
E-mail addresses: suresh.bhargava@rmit.edu.au (S.K. Bhargava), E04781@ems.rmit.edu.au (D.B. Akolekar).

1381-1169/$ – see front matter © 2006 Elsevier B.V. All rights reserved.
doi:10.1016/j.molcata.2006.11.018

(XAFS), and other techniques were employed to evaluate the characteristic behaviour of gold nanoparticles in rare earth materials.

2. Experimental

Supported gold nanoparticles rare earth materials were prepared using the precipitation–deposition/co-precipitation methods [9,10]. Gold nanoparticles were supported on the oxides of europium. dysprosium, samarium oxide, neodymium, gadolinium oxide and lanthanum using the above-mentioned methods. The supported gold nanoparticles materials were prepared by simultaneous precipitation of gold and metal oxide using dilute sodium hydroxide (NaOH)/sodium carbonate (or without NaOH) under an inert atmosphere/by immersing the calcined material in dilute $HAuCl_3$ (<0.2 g/L) solution at 328 K for 7 h (with continuous stirring) and precipitating gold hydroxide using NaOH. After the completion of the preparation process, the precursor is washed, dried at 323 K for 20 h and calcined at 653 K for 4h in helium. During the sample preparation, the gold precursor is deposited into the macropores of the material and precipitated as gold hydroxide. Upon further heating the sample at 653 K, gold hydroxide is reduced to metallic gold. For studying the influence of gold concentration on the properties of gold nanoparticles, different dysprosium and lanthanum (Table 1) containing different loadings of gold nanoparticles were prepared using similar synthesis conditions. The uncalcined and calcined nano-gold rare earth samples were employed in the XAFS TEM and other studies.

The chemicals used in the synthesis of the materials were high purity salts (nitrate/chloride) of europium, dysprosium, samarium, neodymium, gadolinium and lanthanum (Aldrich), sodium hydroxide (BDH) and water based gold chloride solution. The materials were characterized for their chemical composition, phase purity, structure, surface properties and particle size using standard and sophisticated instrumental techniques such as ICP-MS (HP4500 Series 300), XRD (Bruker D8 Advance), BET, TEM (JEOL 2010 at 100 kV), TGA, respectively. The surface area and total-pore volume of the materials were obtained by N_2-dynamic adsorption/desorption technique ($p/p_0 = 0.3$) using a Micromeritics ASAP2000 Instrument. The details of instruments utilized and characterization methods are reported elsewhere [11–13].

Table 1
Chemical composition of gold nanoparticles supported on different rare earth oxide materials

Material type	Product composition (mol%)		Me/Au
	Au	Me	
Au–Eu (A)	1.91	98.09	51.35
Au–Eu (B) (Au–Eu (A) calcined)	1.89	98.11	51.91
Au–Dy (A)	1.88	98.12	51.92
Au–Dy (B) (Au–Dy (A) calcined)	1.85	98.15	53.04
Au–Dy (C)	1.94	98.06	50.55
Au–Dy (D)	1.96	98.04	50.02
Au–Sm	1.84	98.16	53.35
Au–Nd	1.86	98.14	52.8
Au–Gd	1.88	98.12	52.19
Au–La [A]	1.81	98.19	54.3
Au–La [B]	1.89	98.11	51.9
Au–La [C]	1.86	98.14	52.76
Au–La [D]	1.83	98.17	53.6
Au–La [E]	1.79	98.21	54.9

Me: rare earth element.

High-resolution X-ray absorption spectroscopy (XAS) was utilised for investigating the atomic and molecular structures of the supported nanoparticles on rare earth materials [14]. Au L_3-edge EXAFS spectra were recorded in fluorescence mode at the Australian National Beamline Facility (ANBF), Beamline 20B (bending magnet) (2.5 GeV Photon Factory, KEK, Tsukuba, Japan). The excitation energy was selected using water-cooled Si(1 1 1) channel cut crystal monochromator (11 m away from the light source). The beam size of 2 mm (horizontal) × 1 mm (vertical) was controlled with a slit assembly (13 m away from the source). Using a Au foil as an internal standard performed energy calibration and the energy reproducibility was checked from time-to-time. Fluorescence was measured using a Canberra GL0110S 10/36-element Ge array detector. The signal from each array element was passed from the detector, *via* a Canberra Model 2026XA Spectroscopy Amplifier (shaping time 0.25 μs), to a Canberra Model 2030 Single Channel Analyzer, which was set to pass the Au L_3-edge signal to the counting electronics. For all samples, 4/5 scans (scan time, ∼60 min) were taken at the energy range: 11,800–12,800 eV. The fluorescence was normalized to the incident beam flux monitored by an ionization chamber with a 30 cm path length containing standard Ar/Kr mixtures.

The spectra were recorded (in fluorescence mode) at room temperature. Powder samples were pressed into (<0.5 mm thick) pellets supported in an aluminium spacer between Kapton tape windows. The spectra were averaged from 4/5 scans. Averaging, background subtraction, random errors (arising due to noise) and calculation of theoretical EXAFS spectra were performed using the XFIT software package. The model fitting calculations were performed using the XFIT program, where a non-linear least squares procedure is used to fit the model parameters to the observed XAFS [15,16]. XFIT incorporates *ab initio* calculations of the XAFS using the programs FEFF 4.06 for single scattering and FEFF 6.01 for multiple scattering. The parameters such as coordinates of all atoms, Debye–Waller factors, threshold energy etc were varied to optimise agreement between the calculated and observed XAFS. The observed and calculated XAFS were Fourier filtered and the goodness-of-fit parameter and statistical errors were estimated according to the reported methods [15]. The entire chi function was fit. For EXAFS measurements, as prepared (Au–Eu, Au–Dy), calcined (Au–Eu, Au–Dy, Au–Sm, Au–Nd, Au–Gd, Au–La) and different loadings of gold nanoparticles [Au–Dy (A), Au–Dy (B), Au–Dy (C), Au–Dy (D), Au–La (A), Au–La (B), Au–La (C), Au–La (D), Au–La (E)] samples were used.

3. Results and discussion

Table 1 shows the gold nanoparticles containing materials and their gold and respective rare earth element chemical composition. The chemical analysis of the samples showed that the concentration of gold varied (range 2.5–2.7 Au wt%) with the rare earth oxide host structures. The structural analysis confirmed the desired structure and phase purity of the rare earth materials and the presence of gold (fcc) in these materials.

Fig. 1 shows the typical TEM images of the gold nanoparticles on the europium oxide (uncalcined and calcined) samples. For Au–Eu samples, TEM analysis showed the presence of gold in nanoparticulate form, with average nanoparticles size of 2.5 nm for uncalcined Au–Eu sample and the high temperature treatments caused an increase in the gold particle size to 5 nm.

For other rare earth samples, the TEM analysis confirmed the gold particle sizes between 2 and 6 nm for different rare earth element and different loadings of gold nanoparticles. The details of gold particle sizes on the rare earth elements are presented in Table 2. Investigations of the surface characteristics (surface area, pore volume, adsorption/desorption isotherm, pore size and volume distribution) of the gold containing samples (Table 2) suggested that the surface area varies from 29 to 41 m^2/g and the supported rare earth materials are macro-porous in nature.

The gold nanoparticles on various rare earth oxide materials {Au–Eu (A) [Me/Au 51.35], Au–Eu (B) [Me/Au 51.91], Au–Dy (A) [Me/Au 51.92], Au–Dy (B) [Me/Au 53.04], Au–Dy (C) [Me/Au 50.55], Au–Dy (D) [Me/Au 50.02], Au–Sm [Me/Au 53.35], Au–Nd [Me/Au 52.8], Au–Gd [Me/Au 52.19], Au–La [A] [Me/Au 54.3], Au–La [B] [Me/Au 51.9], Au–La [C] [Me/Au 54.6], Au–La [D] [Me/Au 54.2], Au–La [E] [Me/Au 54.86]} were investigated for Au L_3-XAFS in order to elucidate variations in the local environment and structure around the gold atom. EXAFS data for the materials were obtained at RT using the Amby's experimental set-up. X-ray absorption spectra of gold nanoparticles on uncalcined and calcined Au–Eu and Au–Dy (Au–Eu (A) [Me/Au 51.35], Au–Eu (B) [Me/Au 51.91], Au–Dy (A) [Me/Au 51.92], Au–Dy (B) [Me/Au 53.04], Au–Dy (C) [Me/Au 50.55], Au–Dy (D) [Me/Au 50.02]) (Fig. 2 and Table 1) materials exhibits difference in the peak height and fineness in features with the difference being more prominent in uncalcined and calcined samples. Figs. 3 and 4 show the experimental (solid black lines) and theoretical (calculated best fits) (dotted lines) plots of the Au L_3-edge k^3-weighted EXAFS function k^3c (k) of Au–Sm [Me/Au 53.35], Au–Nd [Me/Au 52.8], Au–Gd [Me/Au 52.19], Au–La [A] [Me/Au 54.3], and Au–La [B] [Me/Au 51.9], Au–La [C] [Me/Au 54.6], Au–La [D] [Me/Au 54.2], Au–La [E] [Me/Au 54.86]} samples, respectively. Usually the shorter bond length observed in smaller nanoparticles is due to the lower coordination number and asymmetric distribution of Au (the near-neighbor Au–Au distribution). The high temperature treatment exhibited changes in the feature of XAFS spectra and the peak height. The XAFS spectra (Au L_3-edge) of metallic gold are similar to these gold nanoparticles rare earth samples [17].

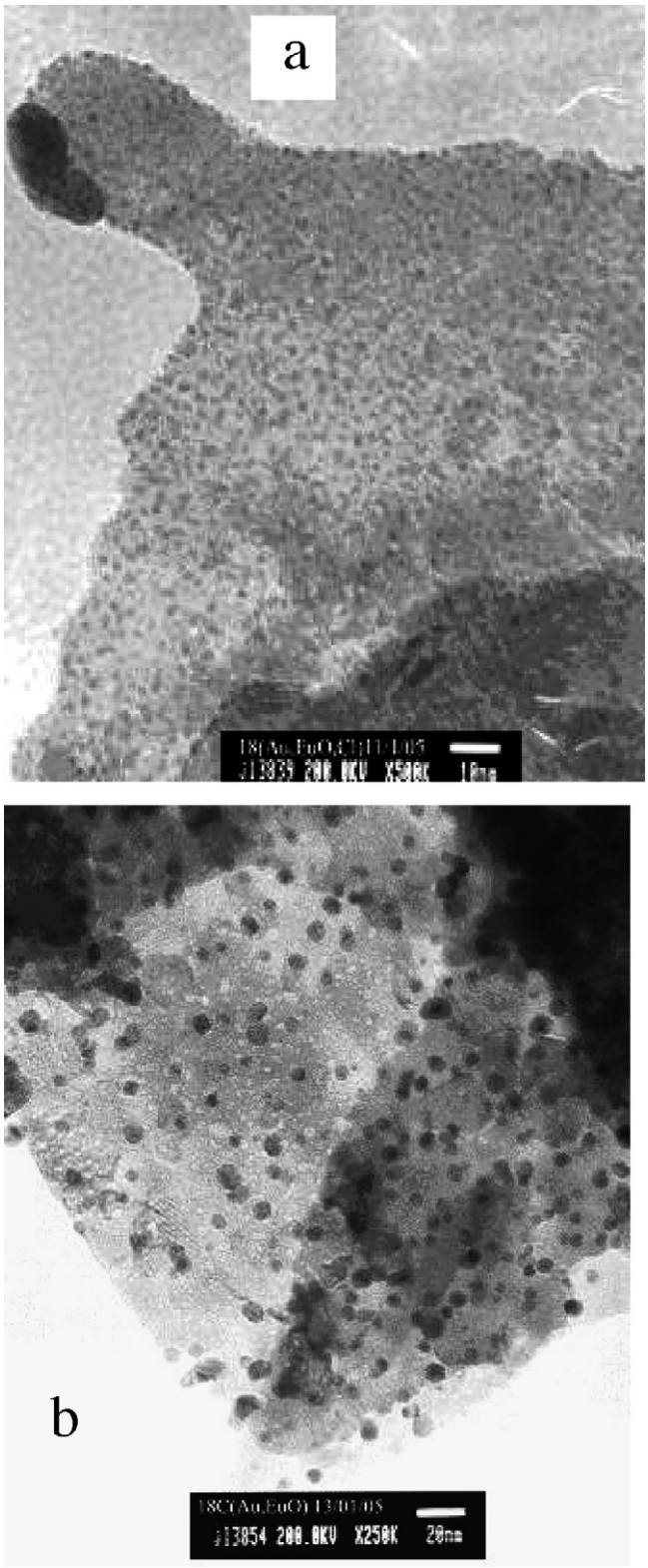

Fig. 1. Typical TEM images of gold nanoparticles supported on rare earth oxide materials: (a) uncalcined Au–Eu and (b) calcined Au–Eu.

Figs. 5–7 show the experimental (solid black lines) and theoretical (calculated best fits) (dotted lines) plots of the Au L_3-edge Fourier transform of gold nanoparticles rare earth samples. For all the samples, the goodness-of-fit value (R) was in the range

Table 2
Particle size and surface characteristics of the gold nanoparticles supported on different rare earth oxide materials

Material type	Gold particle size (on as—prepared samples) (nm)	Surface properties		
		Surface area (m^2/g)	Micropore volume (cm^3/g)	Total pore volume (cm^3/g)
Au–Eu (A)	∼2.5	39	0.002	0.185
Au–Eu (B) (Au–Eu (A) calcined)	∼5–6	41	0.002	0.194
Au–Dy (A)	∼3	33	0.001	0.175
Au–Dy (B) (Au–Dy (A) calcined)	∼5	37	0.002	0.18
Au–Dy (C)	∼3–4	36	0.001	0.18
Au–Dy (D)	∼3–5	35.5	0.002	0.18
Au–Sm	∼3	36	0.001	0.17
Au–Nd	∼4	34	0.001	0.165
Au–Gd	∼3–6	41	0.002	0.20
Au–La [A]	∼2–4	32	0.001	0.16
Au–La [B]	>4	31	0.001	0.16
Au–La [C]	2–3	33	0.001	0.155
Au–La [D]	2–5	30	0.001	0.16
Au–La [E]	3–6	29	0.001	0.15

16.7–21% (Table 3) and the value of the energy E in the fitting procedure varied from −3.3 to −8.2 eV.

Fig. 5(a, c and e) shows the Fourier transforms of uncalcined nano-gold particles containing Eu/Dy supports. The Fourier transforms show that majority of gold species present in the uncalcined Eu and Dy samples is oxidic gold (Au–O) and with very few of metallic gold species. The Fourier transforms (Fig. 5b, d and e) of the calcined Au–Eu and Au–Dy samples shows predominant presence of metallic gold species (Au–Au) (Au–M support). The similarity of XANES and Fourier transforms of uncalcined or calcined Au–Eu and Au–Dy materials

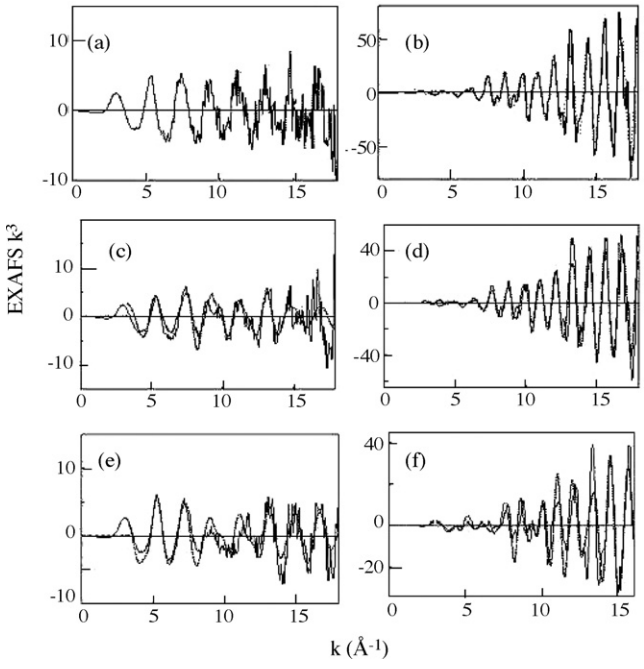

Fig. 2. EXAFS spectrum (Au L_3) of gold nanoparticles on (a) europium (Au–Eu [A]), (b) calcined europium oxide (Au–Eu [B]), (c) dysprosium oxide [Au–Dy (A)] (d) calcined dysprosium [Au–Dy (B)] oxide; (e) dysprosium oxide [Au–Dy (C)]; (f) dysprosium oxide [Au–Dy (D)]. The solid lines are experimental data, and the overlaid dotted lines are the best fits (calculated).

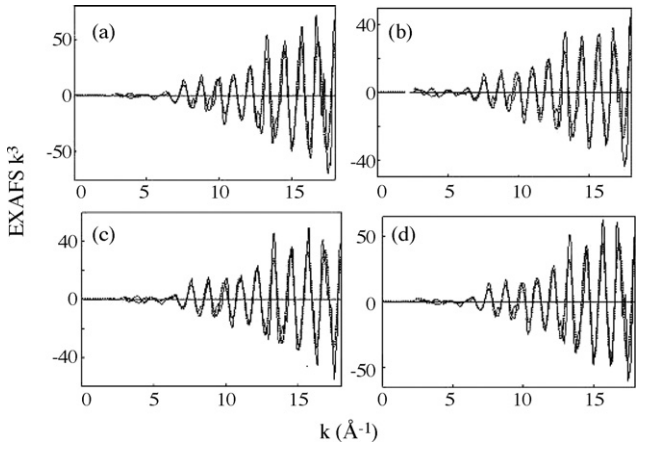

Fig. 3. EXAFS spectrum (Au L_3) of gold nanoparticles on (a) calcined samarium oxide [Au–Sm] oxide; (b) Neodymium oxide [Au–Nd]; (c) gadolinium oxide [Au–Gd]; (d) lanthanum oxide [Au–La (A)]. The solid lines are experimental data, and the overlaid dotted lines are the best fits (calculated).

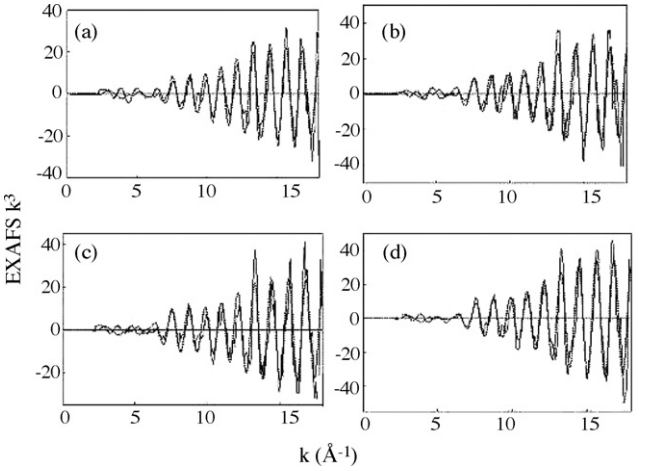

Fig. 4. EXAFS spectrum (Au L_3) of gold nanoparticles on (a) lanthanum oxide [Au–La (B)]; (b) lanthanum oxide [Au–La (C)]; (c) lanthanum oxide [Au–La (D)]; (d) lanthanum oxide [Au–La (E)]. The solid lines are experimental data, and the overlaid dotted lines are the best fits (calculated).

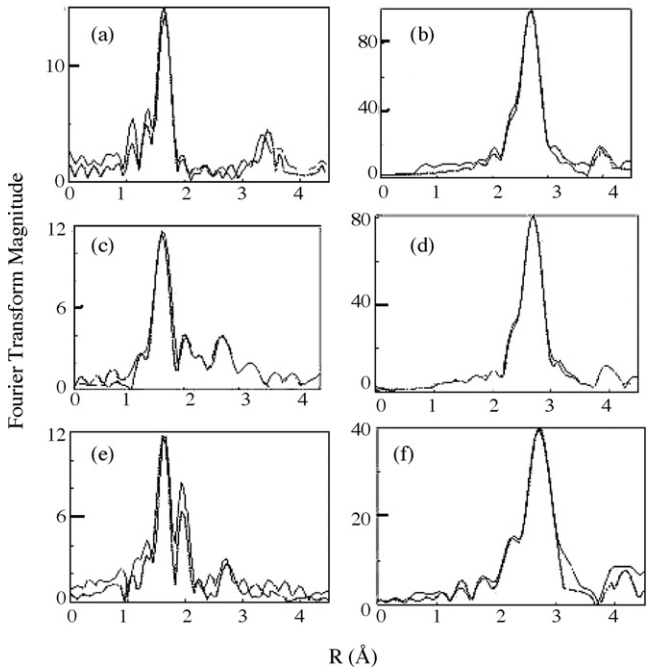

Fig. 5. EXAFS Fourier transforms (Au L_3) of gold nanoparticles on (a) europium (Au–Eu [A]); (b) calcined europium oxide (Au–Eu [B]); (c) dysprosium oxide [Au–Dy (A)]; (d) calcined dysprosium [Au–Dy (B)] oxide; (e) dysprosium oxide [Au–Dy (C)]; (f) dysprosium oxide [Au–Dy (D)]. The solid lines are experimental data, and the overlaid dotted lines are the best fits (calculated).

indicate the local structure around the gold atom is similar despite the elements in the material. On the radial distribution curve, the characteristic profile of metallic gold is easily recognized (Au–Au $\sim 2.6 \pm 0.04$ Å). A signal at about 1.5–1.8 Å observed in the radial distribution curve is characteristic of oxidized gold surrounded by light atoms (mostly short Au–O bond).

The bond length and other parameters (Debye–Waller factor and *R* factor) results obtained from EXAFS analysis for Au–Eu and Au–Dy samples are summarized in Table 3. The signal around 2.2 ± 0.6 Å observed in certain samples can be

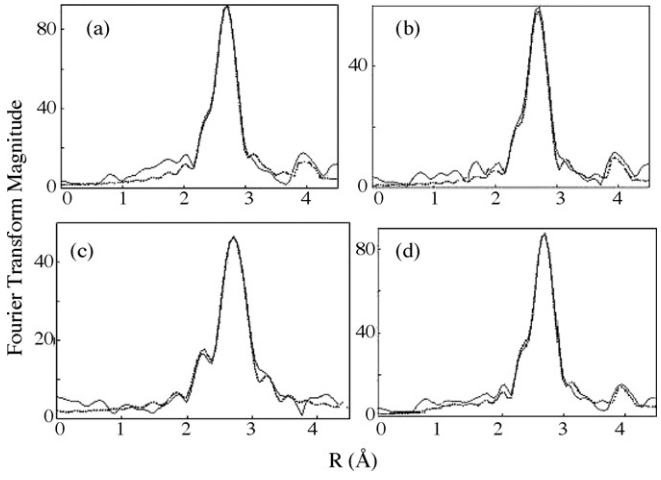

Fig. 6. EXAFS Fourier transforms (Au L_3) of gold nanoparticles: (a) calcined samarium oxide [Au–Sm] oxide; (b) neodymium oxide [Au–Nd]; (c) gadolinium oxide [Au–Gd]; (d) lanthanum oxide [Au–La (A)]. The solid lines are experimental data, and the overlaid dotted lines are the best fits (calculated).

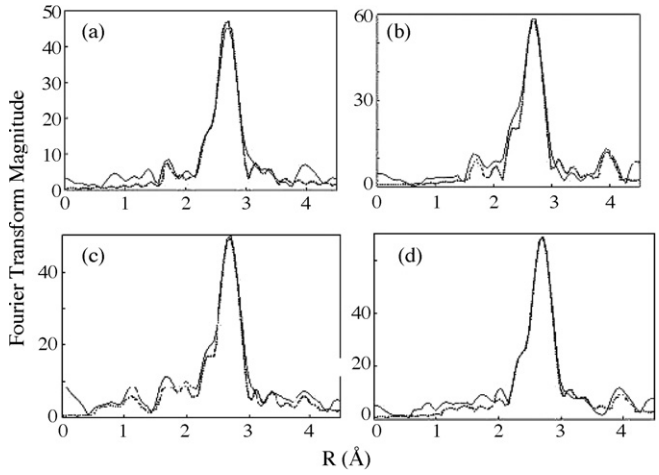

Fig. 7. EXAFS Fourier transforms (Au L_3) of gold nanoparticles on (a) lanthanum oxide [Au–La (B)]; (b) lanthanum oxide [Au–La (C)]; (c) lanthanum oxide [Au–La (D)]; (d) lanthanum oxide [Au–La (E)]. The solid lines are experimental data, and the overlaid dotted lines are the best fits (calculated).

assigned to the binding of Au with the Cl or Au or O or support element (designated as M) depending upon the treatment conditions and support type [10,18]. The observed signal at 2.14 Å in the Au–Eu (A), 2.18 Å in the Au–Dy (A), 2.18 Å in the Au–Dy (C) sample is related to the binding of Au with Cl, while in the high temperature calcined Au–Eu (B), Au–Dy (B), and Au–Dy (D) samples the signal at ~2.14 Å is related to the binding of Au with Au/O/support (M) [17]. The Au–Eu/Dy materials mostly show three to four types of coordination number.

The magnitude of Au–Au and Au–M peaks as well as their relative ratios in radial distribution function slightly varied in different host europium and dysprosium materials. The observed low Au–Au signal at $\sim 2.72 \pm 0.03$ Å indicates the presence of small gold particles [17,18]. In the bulk gold foil, the Au–Au signal was observed at 2.85 Å. The X-ray powder analysis on the gold nanoparticles in the rare earths oxide materials indicated a face centred cube structure of nano-gold particles.

Fig. 6 shows Fourier transform of calcined Au–Sm, Au–Nd, Au–Gd and Au–La samples. Tables 3 and 4 present the bond length and other parameters (Debye–Waller factor and R factor) results obtained from EXAFS analysis for Au–Sm, Au–Nd, Au–Gd, and Au–La samples. The majority of gold species present in these calcined samples are metallic gold species. For the Au–Sm, Au–Nd, Au–Gd and Au–La samples, the goodness-of-fit value (*R*) was in the range 15.5–18.5% (Tables 3 and 4). The Fourier transform results show that the magnitude of Au–O, Au–M and Au–Au and their ratios are different for the gold nanoparticles supported on the Sm, Nd, and Gd and La supports.

Fig. 7 shows Fourier transform of calcined Au–La (B), Au–La (C), Au–La (D) and Au–La (E) samples. These Au–La samples contain different concentrations of nano-gold particles with similar support type. The bond length and other parameters (Debye–Waller factor and *R* factor) results obtained from EXAFS analysis Au–La (B), Au–La (C), Au–La (D) and Au–La (E) samples are presented in Table 4. The majority of gold species present in these calcined samples are metallic gold species. The goodness-of-fit value (*R*) was in the range

Table 3
Data of the atomic distances, Debye–Waller factor and *R* factor of gold nanoparticles supported on different rare earth oxide materials

Material type	Atom type	Bond length (Å)	Debye–Waller factor (Å^2)	*R* factor (%)	Symmetry
Au–Eu (A)	O-Mj	1.57	0.0027 (1)	21.1	fcc
	Cl sh	2.14	0.001 (2)		
	Au*	2.56	0.003 (2)		
	O	1.78	0.0035 (1)	18.6	fcc
Au–Eu (B) (Au–Eu (A) calcined)	Au/M	2.13	0.0041 (1)		
	Au	2.72	0.0033 (2)		
Au–Dy (A)	O-Mj	1.58	0.0026 (1)	20.3	fcc
	Cl sh	2.18	0.001 (2)		
	Au*	2.61	0.003 (2)		
	O	1.76	0.003 (1)	16.6	fcc
Au–Dy (B) (Au–Dy (A) calcined)	Au/M	2.14	0.004 (2)		
	Au	2.73	0.005 (1)		
Au–Dy (C)	O	1.56	0.002 (1)	18.95	fcc
	O	1.89	0.0035 (1)		
	Cl	2.18	0.0014 (2)		
	Au	2.75	0.0040 (2)		
Au–Dy (D)	O*	1.59	0.004 (1)	18.4	fcc
	Au/M	2.14	0.0036 (3)		
	Au	2.75	0.004 (2)		
Au–Sm	O	1.74	0.0033 (1)	18.5	fcc
	Au/M	2.13	0.0040 (1)		
	Au	2.73	0.0031 (2)		
Au–Nd	O	1.78	0.0045 (2)	16.5	fcc
	Au/M	2.15	0.005 (1)		
	Au	2.74	0.0025 (2)		

(M = O/Cl/Me) A_i = Debye–Waller factor (Å^2) of the *i*th shell; *minor shoulder peak.

17.8–19.9% for the Au–La (B), Au–La (C), Au–La (D) and Au–La (E) samples. Slight variations in the magnitude of Au–O, Au–M and Au–Au and their ratios were observed for these samples.

TEM measurements showed that the gold particle size increases up to certain levels with the treatment temperature (above 873 K). The increase in particle size is due to gold particle aggregation at higher temperature. Fig. 8 shows the

Table 4
Data of the atomic distances, Debye–Waller factor and *R* factor of gold nanoparticles supported on different rare earth oxide materials

Material type	Atom type	Bond length (Å)	Debye–Waller factor (Å^2)	*R* factor (%)	Symmetry
Au–Gd	O	1.78	0.003 (2)	15.5	fcc
	Au/M	2.14	0.004 (1)		
	Au	2.78	0.0034 (2)		
	O	1.80	0.003 (1)	16.9	fcc
Au–La [A]	Au/M	2.12	0.004 (2)		
	Au	2.74	0.005 (1)		
Au–La [B]	O	1.80	0.003 (1)	19.9	fcc
	Au/M	2.15	0.002 (2)		
	Au	2.74	0.0040 (2)		
Au–La [C]	O*	1.71	0.004 (1)	19.5	fcc
	Au/M	2.13	0.0036 (3)		
	Au	2.74	0.005 (2)		
Au–La [D]	O*	1.69	0.003 (1)	18.2	fcc
	Au/M	2.12	0.004 (3)		
	Au	2.75	0.006 (2)		
Au–La [E]	O*	1.75	0.0035 (1)	17.8	fcc
	Au/M	2.14	0.0046 (3)		
	Au	2.76	0.0045 (2)		

(M = O/Cl/Me) A_i = Debye–Waller factor (Å^2) of the *i*th shell; *minor shoulder peak.

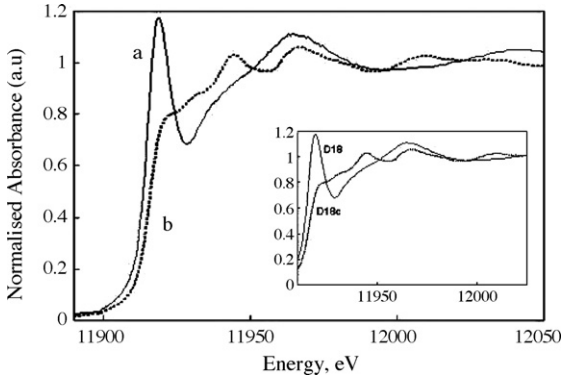

Fig. 8. Au L_3-edge XANES spectra of gold nanoparticles on (a) europium (Au–Eu [A]) and (b) calcined europium oxide (Au–Eu [B]).

Au L_3-edge XANES spectra of gold nanoparticles on uncalcined Au–Eu and calcined Au–Eu samples. The site symmetry, spin state, atomic position of neighbours and oxidation state (edge shift-binding energy shift) of the metal are important information given by XANES. The XANES spectrum of the uncalcined Au–Eu sample is different from the calcined Au–Eu samples.

Fig. 9 shows Au L_3-edge XANES spectra of gold nanoparticles on as prepared Au–Dy (A), calcined Au–Dy (B) and Au–Dy with higher gold concentration. The XANES spectra were background corrected. In Fig. 9, the XANES data shows significant variations for the gold nanoparticles on as prepared Au–Dy (A), calcined Au–Dy (B) and Au–Dy with higher gold concentration. Au L_3-edge XANES spectra of Au–Sm, Au–Nd, Au–Gd, and Au–La samples and analysis of Au–La (B), Au–La (C), Au–La (D) and Au–La (E) samples are presented in Figs. 10 and 11, respectively. The XANES clearly indicates oxidized as well as reduced Au species. Figs. 8–11 show four distinct edge features. In the "white line" peak (∼11928 eV) is suppressed in the XANES spectra of Au–rare earth oxide samples due to full occupancy of d states for gold. The peak around 11940 eV is a weak feature but mostly present in bulk gold, gold nanoparticles, etc., while the two peaks between 11,940 and 11,980 eV are more structure dependent. The peaks after

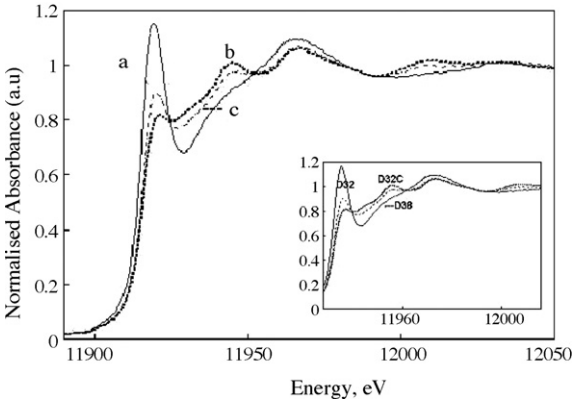

Fig. 9. Au L_3-edge XANES spectra of gold nanoparticles: (a) dysprosium oxide [Au–Dy (A)]; (b) calcined dysprosium [Au–Dy (B)] oxide; (c) dysprosium oxide [Au–Dy (D)].

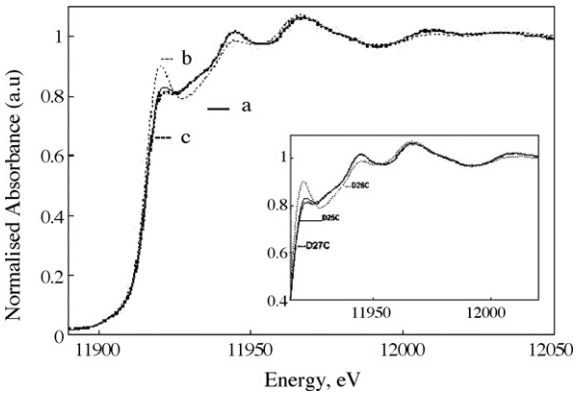

Fig. 10. Au L_3-edge XANES spectra of gold nanoparticles on (a) calcined samarium oxide [Au–Sm] oxide; (b) neodymium oxide [Au–Nd]; (c) gadolinium oxide [Au–Gd].

11,940 eV represent the extended local structure around the absorbing atom [19]. It is interesting to note that the XANES spectrum for gold nanoparticles present in different rare earth oxide samples is different. The peaks in the 11,925–11,980 eV regions suggest that factors such as the concentration of gold nanoparticles and host element type structure influences the XANES.

The XANES pattern of the heat-treated Au rare earth samples is different from that of as-prepared Au–rare earth samples. The uncalcined Au–rare earth samples exhibits a strong peak at 11,926 eV and the intensity of this peak further decreases with temperature. The 11,926 eV peak is not observed in the calcined Au–rare earth samples. The uncalcined Au–rare earth samples mostly contain Au–O species, which further gets converted to various Au–Au/Au–M species at higher temperatures. The intensity and width of these XANES peaks can be related [20,21] to the number of neighbours surrounding each gold atom as well as to the size of gold particle. In XANES spectra (Figs. 8–11) including XAS, the intense and defined peaks (in higher XANES region) are consistent with the reported results on gold nanoparticles [19].

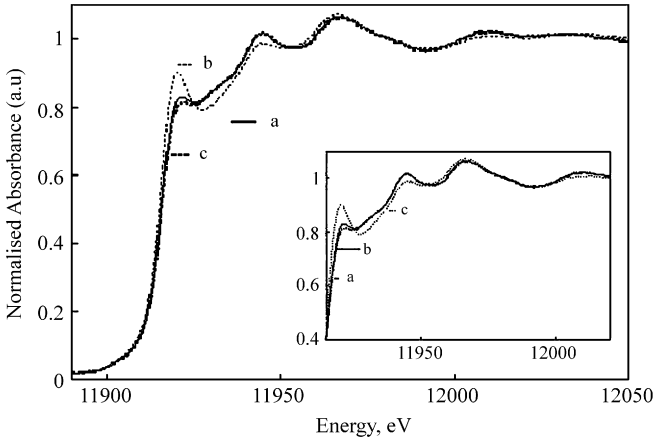

Fig. 11. Au L_3-edge XANES spectra of gold nanoparticles on (a) lanthanum oxide [Au–La (B)]; (b) lanthanum oxide [Au–La (C)]; (c) lanthanum oxide [Au–La (D)]; (d) lanthanum oxide [Au–La (E)].

4. Conclusions

Using the precipitation–deposition/co-precipitation methods, nanoparticles gold with different sizes, uniformity and concentration could be prepared in the rare earth oxide support materials such as europium, dysprosium, samarium, neodymium, gadolinium and lanthanum materials. On the rare earth oxide supports, the dispersion and size of gold nanoparticles are different and size of gold nanoparticles vary from 2 to 6 nm.

On the uncalcined Au–rare earth (Au–Eu (A), Au–Dy (A) Au–Dy (C)) samples, the XAFS/XANES and Fourier Transform show the presence of mainly oxidic gold species while on the calcined Au–rare earth samples, metallic gold species (either Au–Au or Au–Me) are predominant. In these rare earth samples, variation in the magnitude of Au–O/Au–Au in the radial distribution function is also observed. The host support type (Eu/Dy/Sm/Nd/Gd/La) and structure, particle size, metal concentration, and calcination temperature influences the characteristics of the nano-gold particles as indicated by the changes in the XAFS and XANES. The gold nanoparticles in different Eu/Dy/Sm/Nd/Gd/La support structures exhibits different Au bond length and the Au–Au signal at $\sim 2.73 \pm 0.03$ Å indicates the presence of small gold nanoparticles.

Acknowledgements

We gratefully acknowledge the financial support of the Australian Synchrotron Research Program (Australian Nuclear Science and Technology Organization, ANSTO), Sydney. We thank ANBF (Australian National Beamline Facility, 20B) team, Photon Factory of the National Laboratory for High Energy Physics (KEK), Tsukuba, Japan for assistance and facility support.

References

[1] M. Haruta, Catal. Today 36 (1997) 153.
[2] T. Kobayashi, M. Haruta, S. Tsubota, H. Sano, Sens. Actuators B 1 (1990) 222.
[3] V.P. Zhdanov, B. Kasemo, Surf. Sci. Lett. 511 (2002) 23.
[4] M. Haruta, Catal. Surveys Jpn. 1 (1997) 61.
[5] M. Haruta, N. Yamada, T. Kobayashi, S. Iijima, J. Catal. 115 (1989) 301.
[6] N.M. Gupta, A.K. Tripathi, J. Catal. 187 (1999) 343.
[7] M. Haruta, T. Kobayashi, H. Sano, N. Yamada, Chem. Lett. 405 (1987).
[8] K.-C. Wu, Y.-L. Tung, C.-C. Dai, United States Patent Application 20040127353 (July 1, 2004).
[9] S. Tsubota, M. Haruta, T. Kobayashi, A. Ueda, Y. Nakahara, G. Poncelet, et al. (Eds.), Preparation of Catalysts V, Elsevier Science B.V., 1991, p. 695.
[10] D.B. Akolekar, S.K. Bhargava, J. Synchrotron Rad. 11 (3) (2004) 284.
[11] D.B. Akolekar, J. Catal. 143 (1993) 227.
[12] D.B. Akolekar, A. Chaffee, R.F. Howe, Zeolites 19 (1997) 359.
[13] D.B. Akolekar, S.K. Bhargava, Stud. Surf. Sci. Catal. 105 (1998) 755.
[14] D.C. Koningsberger, R. Prins, in: D.C. Koningsberger, R. Prins (Eds.), X-ray Absorption, John Wiley & Sons, New York, 1988.
[15] P.J. Ellis, H.C. Freeman, J. Synchrotron Rad. 2 (1995) 190.
[16] XFIT for Windows '95; Australian Synchrotron Research Program: Sydney, 1996.
[17] D. Guillemot, M. Polisset-Thfoin, D. Bonnin, V.Y. Borovkov, Proceedings of the 12th International Zeolite Conference, Materials Research Society, USA, 1999, p. 2079.
[18] H. Kageyamma, T. Tsubota, N. Kamijo, M. Haruta, Jpn. J. Appl. Phys. 32 (Suppl. 32-2) (1993) 445.
[19] R.E. Benfield, V.M. Grandjean, Kroll, R. Pugin, T. Sawitowski, G. Schmid, J. Phys. Chem. B 105 (2001) 1961.
[20] G.N. Greaves, P.J. Durham, G. Diakun, P. Quinn, Nature 294 (1981) 139.
[21] D. Bazin, D. Sayers, J.J. Rehr, C. Mottet, J. Phys. Chem. 101 (1997) 5332.